

# **Separate 20-day and 30-day Tropical Instability Waves in subsurface temperature observations**

JOHN M. LYMAN, GREGORY C. JOHNSON, AND WILLIAM S. KESSLER

*NOAA/Pacific Marine Environmental Laboratory, Seattle, Washington 98115 USA*

Submitted to Journal of Physical Oceanography:

September 21, 2004

*Corresponding author address:*

John M. Lyman, Pacific Marine Environmental Laboratory, NOAA/R/PMEL, 7600 Sand Point  
Way, Seattle, WA 98115 (email:John.Lyman@noaa.gov)

## ABSTRACT

Tropical Instability Waves (TIWs) within a half-degree of the equator in the Pacific Ocean have been consistently observed in meridional velocity with periods around 20 days. On the other hand, near  $5^{\circ}\text{N}$  TIWs have been observed in sea surface height (SSH), thermocline depth, and velocity to have periods of near 30 days. Tropical Atmosphere Ocean (TAO) project moored velocity at the equator and temperature time series along  $140^{\circ}\text{W}$  are used to investigate the spatial and temporal structure of TIWs during 3 years of La Niña conditions from 1998 through 2001. Rather than one broad-banded (in frequency) TIW, the variability at  $140^{\circ}\text{W}$  consists of two distinct TIWs with periods of 17 and 33 days. As predicted by modeling studies, the 17-day TIW variability is shown to occur not only in meridional velocity at the equator but also in subsurface temperature at  $2^{\circ}\text{N}$  and  $2^{\circ}\text{S}$ , while the 33-day TIW variability is observed in subsurface temperature at  $5^{\circ}\text{N}$ . These two TIWs are shown to have characteristics similar to a Yanai wave/surface trapped instability and an unstable first meridional mode Rossby wave, respectively.

## 1. Introduction

In the Pacific, Tropical Instability Waves (TIWs) have classically been characterized by meanders in the sea surface temperature (SST) front just north of the equator. These meanders, as observed in early satellite SST images, were estimated to have 25-day periods and 1000-km wavelengths (Legeckis 1977). The description of TIWs has since been broadened to include additional observations of sea surface height (SSH; Miller et al. (1985); Malardé et al. (1987); Musman (1989); Périgaud (1990); Chelton et al. (2004)), in situ velocity (Halpern et al. 1988; Bryden and Brady 1989; Qiao and Weisberg 1995; McPhaden 1996; Kennan and Flament 2000), wind stress (Xie et al. 1998; Chelton et al. 2001; Hashizume et al. 2001), ocean color (Strutton et al. 2001), in situ temperature (McPhaden 1996; Flament et al. 1996; Kennan and Flament 2000) and SST (Legeckis et al. 1983; Legeckis 1986; Pullen et al. 1987; Chelton et al. 2004; Contreras 2001). These investigations have expanded the definition of TIWs to include variability occurring north and south of the equator with a large range of periods (15-40 days) and wavelengths (700-1600 km).

Observations of TIWs in the equatorial Pacific from in situ measurements of subsurface temperature and velocity along with satellite measurements of SSH have fallen into two categories that vary geographically and are dependent on the observed field. The first has periods around 15-23 days, occurs within a degree of the equator, and is most prominent in meridional velocity (Halpern et al. 1988; Bryden and Brady 1989; Qiao and Weisberg 1995; McPhaden 1996). The other has periods around 28-35 days and has been observed in SSH, thermocline depth, and velocity centered about 5°N (Miller et al. 1985; Malardé et al. 1987; Musman 1989; Périgaud 1990; McPhaden 1996; Flament et al. 1996; Kennan and Flament 2000; Chelton et al. 2004). Through-

out this paper, variability with periods between 15-23 days is referred to as 20-day variability. Likewise, variability with periods between 28-35 days is referred to as 30-day variability.

Nonlinear numerical models and linear stability analyses of the equatorial Pacific reproduce aspects of either the 30-day variability (Philander 1978; Cox 1980; Lyman et al. 2004), or both the 30-day and the 20-day variability (McCreary and Yu 1992; Proehl 1996; Donohue and Wimbush 1998; Masina et al. 1999a; Seidel and Giese 1999), and sometimes contain other instabilities that fall outside of these two categories. The structure of the 20-day variability in these models, although not always shown, has an off-equator signal in SSH and in situ subsurface temperature separate from the 30-day variability. We are not aware of direct evidence for these 20-day signatures in past analyses of either SSH or subsurface temperature.

Experimental studies of TIW energetics support the idea that TIW variability on and off the equator are different. Luther and Johnson (1990) investigated TIW variability from shipboard Acoustic Doppler Current Profilers (ADCP) and CTD sections from the Hawaii-Tahiti Shuttle during the North Pacific Experiment. The low temporal resolution of the data set restricted the study to examining the seasonality and spatial structure of the eddy-mean flow interaction, where eddies were considered to be all variability with periods less than 120 days. They found three regions of TIW energy transfer. The first region is between the Equatorial Undercurrent (EUC) and the north branch of the South Equatorial Current (SECN) where mean kinetic energy is converted to eddy kinetic energy. The second region is at the Equatorial Front (EF) where mean potential energy is converted to eddy potential energy. The last region is in the thermocline near the North Equatorial Countercurrent (NECC) where mean kinetic energy is converted to eddy potential energy.

Drifters deployed in the equatorial Pacific have also shown separate regions of eddy-mean

flow interactions. Hansen and Paul (1984) deployed 20 satellite-tracked Argos surface drifters in the summer of 1979 in a region from 125°W to 105°W and 10°S to 10°N. From these data, they were able to show that the surface shear between the EUC and the SECN was the major source of energy for the instabilities. However, there was also energy transfer at the surface from shear between the NECC and the SECN, along with a significant amount of baroclinic energy transfer.

Baturin and Niiler (1997) examined the life cycle of TIWs by separating data from numerous surface drifters in the equatorial Pacific into two regions with dimensions of 20° in longitude by 20° in latitude centered on 0°N, 110°W and 0°N, 140°W. They estimated the meridional heat flux, momentum flux, and energetics, and found that the maximum eddy fluxes occur in October and the maximum kinetic energy production occurs between the NECC and the SECN. There also appeared to be a region of barotropic energy conversion between the EUC and the SECN at 110°W; however the large divergence at the surface near the equator limited the sampling such that they were unable to estimate this term at 140°W. The long time series allowed for the creation of an index of TIW amplitudes which showed increased TIW activity during La Niña years and decreased TIW activity during El Niño years.

Experimental studies using moored current measurements capable of diagnosing eddy-momentum fluxes in the equatorial Pacific have been confined to within a 1° of the equator (Bryden and Brady 1989; Qiao and Weisberg 1995, 1998). During the Tropical Instability Wave experiment (TIWE) from May 12, 1990, to June 18, 1991 Qiao and Weisberg (1998) analyzed the upper 250 m of the TIW signal, showing that barotropic energy conversion from the shear between the EUC and the SECN was responsible for the onset of the TIWs. However, the limited meridional extent of the moorings made it impossible to address the question of the importance of the NECC.

Observational evidence of two separate forms of TIW variability with different latitudinal

structures was shown in Kennan and Flament (2000). During a large-scale survey that was conducted in November of 1990 between 1°S and 7°N, they observed an individual Tropical Instability Vortex. Their analysis included ship CTD surveys with a towed platform (SeaSoar), ship-board ADCP sections, Argos-tracked surface drifters, TAO mooring data, and infrared satellite images of SST. The rich array of data allowed for a three dimensional picture of what the authors describe as a vortex 500 km in diameter. The feature was highly nonlinear and traveled west between the shear of the NECC and SECN at  $0.3 \text{ m s}^{-1}$ , gaining energy from barotropic energy conversion between the SECN and the NECC (Kennan 1997). A latitudinal variation in phase speed near the equator suggested a different physical phenomenon existed between the EUC and the SECN.

This paper revisits the analysis of McPhaden (1996) that investigated the structure of TIWs during 1988-1989 using temperature data from six moorings that were part of the Tropical Atmosphere-Global Ocean (TOGA)-Tropical Atmosphere Ocean (TAO)/ North Equatorial Countercurrent (NECC) array. These moorings were located along 140°W between 2°S to 9°N. Velocity data from the moorings at 0° and 7°N were also analyzed. The maximum temperature variance occurred in the thermocline between 5°N and 7°N while maxima in the SST variance occurred between 2°N and 5°N. The TIW variability at 140°W was in geostrophic balance with sea level, had 15-50 day periods, and an estimated 750-1150 km wavelength. McPhaden (1996) proposed that the differences in periods between 20-day meridional velocity at the equator observed by Halpern et al. (1988) and the 25-day SST near the equator from Legeckis (1977) could be an effect of a red shift in the temperature spectra due to advection.

Unlike McPhaden (1996), this analysis separates 20 and 30-day TIW variability in subsurface temperature from TAO moorings located at 140°W by looking at a 3-year time series during 3 years of La Niña conditions beginning in April 1998. The most notable difference in the

present study is the isolation of the latitudinal structure of the 20-day variability in temperature that has maxima at  $\pm 2^\circ$  from the equator and is correlated with meridional velocity on the equator. The structure of the 20-day subsurface temperature variability presented here provides further observational evidence for the 20-day variability found in both linear and non-linear models of TIWs. The 20-day variability in subsurface temperature and velocity is shown to be observationally and physically distinct from the 30-day variability. The 20-day variability resembles a Yanai wave/surface trapped instability and the 30-day variability an unstable first-meridional, first-vertical mode Rossby wave. The dynamical differences of the Yanai wave and the unstable first-meridional mode Rossby wave account for differences in period and the distinct latitudinal structure of 20-day and 30-day TIWs.

Section 2 describes the TAO mooring data and filtering. Section 3 takes a detailed look at the latitudinal structure of the TIW variability at  $140^\circ\text{W}$ , separating 20 and 30-day variability. Section 4 discusses possible sources of both the 20 and 30-day TIW variability. Section 5 compares the structure of a Yanai wave in the presence of a mean current with the observed structure of the 20-day TIW variability in temperature and velocity. The results are summarized and discussed in section 6.

## 2. Data and analysis techniques

Here we use temperature and velocity measurements from the TAO array (McPhaden et al. 1998) along  $140^{\circ}\text{W}$  to investigate TIW variability. At  $140^{\circ}\text{W}$  the TAO array consists of seven moorings: six ATLAS (Autonomous Temperature Line Acquisition System) moorings located at  $5^{\circ}\text{S}$ ,  $2^{\circ}\text{S}$ ,  $0^{\circ}\text{N}$ ,  $2^{\circ}\text{N}$ ,  $5^{\circ}\text{N}$  and  $9^{\circ}\text{N}$  and one acoustic Doppler current profiler (ADCP) mooring on the equator (Figure 1). Each ATLAS mooring at  $140^{\circ}\text{W}$  has 11 thermistors located at depths of 1, 20, 40, 60, 80, 100, 120, 140, 180, 300 and 500 meters. Temperatures are recorded every ten minutes and then averaged daily. The subsurface upward-looking ADCP nominal bin width and pulse length are set to 8 meters. These data are then linearly interpolated to a regular grid with 5-meter depth intervals. Velocities are recorded every hour and then averaged daily.

FIG. 1

Persistent La Niña conditions were present from April 1998 to April 2002 (Figure 2). This period provides a three-year record of TIW activity in the central Pacific which can be used to analyze the frequency content of TIWs with greater precision than previously possible (Baturin and Niiler 1997). During this time period gaps of a day to months exist in the velocity and temperature records. Gaps from 1-4 days, short with respect to the TIW period, are filled by linear interpolation, while longer gaps are unaltered. TIW variability is then separated by filtering the resulting time-series so that periods between 10-60 days are retained. This filtered time-series is used throughout this analysis unless otherwise stated.

FIG. 2

In section 3 the coherent variability at  $140^{\circ}\text{W}$  in velocity and temperature is described by a Hilbert complex empirical orthogonal function (CEOF) analysis. CEOFs separate spatial and temporal variability into orthogonal modes which have both amplitude and phase. Unlike the velocity data, the temperature data have significant gaps, which are handled following Davis (1976). In



that paper, the empirical orthogonal function (EOF) time-series is estimated by minimizing the estimated square error (ESE). Times when the ESE was more than 30% of the variance were treated as missing in the time-series.

The power spectral density (PSD) of the CEOF time series are computed by breaking the time series into one-year sections with 50% overlap and then windowing each section with a Hanning window. The power spectral densities of the resulting sections are then averaged, increasing the degrees of freedom (Emery and Thomson 1997). In the case of the first CEOF of temperature, the first one-year section of the time series was not used because it contains missing values.

### 3. The structure of TIWs at 140°W

The strong TIW oscillations present along 140°W are obvious in time-depth plots of temperature at 5°N and 2°S and filtered velocity at the equator during the 1999-2000 TIW season (Figure 3). In this year, which is representative of the three year record and consistent with previously observed TIW seasonality, TIW variability begins in July and abruptly ends in March. The equatorial TIW velocity signal is dominated by the meridional velocity which has a range of more than  $\pm 80$  cm/sec and the thermocline makes large undulations of more than 100 meters at 5°N. The TIW signal is present below the thermocline in both meridional velocity on the equator and temperature at 5°N and 2°S. Periodicity of thermocline depth at 2°S and velocity at the equator is visibly shorter than that of the thermocline depth at 5°N.

FIG. 3

The period of meridional velocity over the 3-year time-span from 1998-2001 is slightly different than previously reported by Qiao and Weisberg (1995) during the TIWE time period from 1990-1991. Figure 4 contours the spectra with depth of filtered meridional velocity for both the 1998-2001 time period (thick lines) and the TIWE time period (thin lines). To treat the two data sets similarly the one year TIWE time series has been band averaged over 3 spectral estimates, while the spectral estimates from the 1998-2001 period were computed according to section 2. The TIWE time-span shows a clear spectral peak at 21 days (500 hours) as previously reported, while the 1998-2001 time period has a peak near 17 days. Both 17 and 21-day periods are in the range for 20-day TIWs produced in models (McCreary and Yu 1992; Proehl 1996; Donohue and Wimbush 1998; Masina et al. 1999a; Seidel and Giese 1999). This small variation in period is likely due to the changing background conditions (Johnson et al. 2002) that are responsible for generating TIWs.

FIG. 4

*a. Velocity variability at the equator*

The amplitude of the filtered velocity variance is surface-intensified, with a meridional variance that is more than twice that of the zonal component (Figure 5). The first CEOF dominates, explaining 63% of the filtered variance. Its amplitude time-series has a seasonal modulation ramping up in July-August and then dissipating in March (Figure 6), consistent with previous TIW analyses. The linear increase of phase, with occasional pauses occurring only at times when the amplitude time-series is small, is characteristic of a periodic signal. These breaks in the phase make it difficult to determine the period of the CEOF from only the phase. Therefore, the period of a CEOF is determined from the PSD of the real part of the CEOF time series (bottom panel Figure 6). For the first CEOF the PSD shows a narrow-banded process with a period of about  $17 \pm 1$  days, where the frequency resolution is based on the one-year record length (Figure 7). The second CEOF explains 17% of the variance, and is broad-banded (Figure 7). Its amplitude time series is inconsistent with the seasonality of TIWs during the three year record. For these reasons, the rest of the analysis will focus on the first mode CEOF.

FIG. 5

FIG. 6

FIG. 7

The first CEOF is surface trapped and dominated by meridional velocity (Figure 8). It explains almost all of the meridional velocity variance above 80 meters and 40-50% below the thermocline. However, it only describes a fraction of the zonal velocity variance at the surface and nearly none at depth. The Reynolds stresses associated with this mode (Figure 8, lower right panel) are on the same order as those reported by Luther and Johnson (1990) and imply a barotropic conversion of energy at the surface. The prominent 17-day, surface-trapped signal dominated by meridional velocity seen in this CEOF mode is similar to previous analyses of observed velocity at  $0^\circ\text{N}$ ,  $140^\circ\text{W}$  (Halpern et al. 1988; Bryden and Brady 1989; Qiao and Weisberg 1995; McPhaden 1996).

FIG. 8

*b. Temperature variability*

The temperature variance along 140°W has maxima at 5°N and 2°S which occur at the thermocline (Figure 9). As was done for the velocity, the temperature variance is expanded in terms of CEOFs.

FIG. 9

Like the first CEOF of velocity, the amplitude time-series for the first and second CEOF of temperature have annual modulations consistent with the observed TIW season (Figure 10). The linear phase increase of both the first and second CEOFs demonstrates that these modes represent periodic signals. As in the case of velocity, there are breaks in the phase time series that occur when the amplitude time series is small. Therefore the period is determined from the PSD of the real part of the CEOF time series (Figure 10, bottom panel). The first and second CEOFs are narrow banded with distinct periods of  $33 \pm 3$  and  $17 \pm 1$  days respectively, where the frequency resolution is based on the one-year record length (Figure 11).

FIG. 10

FIG. 11

The first temperature CEOF has maxima at 5°N and 2°S that are in phase across the equator and much larger north of the equator (Figure 12 top panels). This mode explains most of the variance in the thermocline at 5°N and 22% of the total variance. The large amplitude at 5°N and the 33 day period of this mode are similar to previous analyses of temperature and SSH near 5°N (Miller et al. 1985; Malardé et al. 1987; Musman 1989; Périgaud 1990; Flament et al. 1996; Kennan and Flament 2000; Chelton et al. 2004) and are almost identical to the first mode CEOF of temperature from McPhaden (1996).

FIG. 12

The second CEOF has a structure not previously observed, to our knowledge (although previously modeled), in subsurface temperature or SSH. This mode has maxima at 2°N and 2°S which are out of phase and larger south of the equator. It explains most of the variance in the thermocline

at  $2^{\circ}\text{S}$  and 18% of the total variance (Figure 12). The 17-day period of this mode is the same as the period of the first velocity CEOF at the equator. The lagged cross-correlation of the time-series of the first CEOF of velocity and the second CEOF of temperature shows that velocity time-series leads temperature time-series by 4.25 days (Figure 13). When the spatial phases shown in Figures 8 and 12 are considered, the lag is equivalent to meridional velocity on the equator at the surface leading temperature at  $2^{\circ}\text{S}$  by approximately  $90^{\circ}$ . These combined characteristics of the first CEOF of velocity and the second CEOF of temperature make up the 20-day TIW observed from the TAO moorings at  $140^{\circ}\text{W}$ .

**FIG. 13**

The possible generation mechanisms for the 20-day TIW observed in temperature and velocity and the 30-day TIW observed in temperature are discussed in section 4. In section 5, we will show the characteristics of the 20-day TIW, with the exception of the surface intensified Reynolds stress, are almost identical to a stable Yanai wave in the presence of a mean flow.

#### 4. Possible sources of 30- and 20-day TIWs

Because only equatorial velocity data are available, direct diagnosis of the energetics of the two different TIW signals is not possible. Some aspects of energetics, however, can be inferred from similarities to known unstable solutions computed from previous linear stability analyses.

Several linear models are capable of producing TIWs (Philander 1978; McCreary and Yu 1992; Proehl 1998; Lyman et al. 2004). All of these analyses linearize the equations of motion about a geostrophically balanced mean zonal current, assume a solution of a zonally propagating wave, and then solve the resulting eigenvalue problem looking for unstable solutions.

##### *a. 30-day TIW*

The structure of the first temperature CEOF most closely resembles solutions from Lyman et al. (2004). They linearized the equations of motion about a mean current obtained from the Parallel Ocean Climate Model (POCM) and then projected the state variables onto the set of vertical baroclinic eigenfunctions. The most unstable solution from Lyman et al. (2004) is identified as an unstable first vertical mode ( $n=1$ ), first meridional mode ( $m=1$ ) Rossby wave with maxima at  $5^{\circ}\text{N}$  and  $2^{\circ}\text{S}$ . As in the case of the first CEOF of temperature (Figure 12), the unstable Rossby wave has in phase maxima north and south of the equator that are larger in the north, a period of 31 days (Figure 14 top panel) and almost no meridional velocity on the equator. The maximum amplitudes of the observed first CEOF are slightly deeper, and larger in the south than the modeled unstable

**FIG. 14** Rossby wave.

The striking similarity between the observed first CEOF of temperature and the modeled unstable Rossby wave suggests that this wave is a useful description of the 30-day TIW. The unstable

Rossby wave is generated primarily by barotropic instability, gaining its energy from the shear between the SECN and the NECC (Lyman et al. 2004). This shear has also been observed to be an important contributor to TIWs (Luther and Johnson 1990; Baturin and Niiler 1997; Kennan 1997). Non-linear models also find barotropic instabilities in the SECN-NECC shear to be a source of the 30-day variability (Cox 1980; Donohue and Wimbush 1998). These results lead to the conclusion that barotropic instability in the SECN-NECC shear is a likely mechanism for the generation of the 30-day variability observed in temperature.

It should be noted that Cox (1980), Luther and Johnson (1990), Donohue and Wimbush (1998), and Lyman et al. (2004) also found significant contributions from baroclinic energy conversions between  $2^{\circ}\text{N}$  and  $6^{\circ}\text{N}$ . In a non-linear numerical model of the equatorial Pacific Masina et al. (1999b) found baroclinic instability to be the major source of instabilities in this region. However, she warned that the unrealistically weak NECC in her model could be the reason for the stable SECN-NECC shear and the dominance of baroclinic instability.

#### *b. 20-day TIW*

The characteristics of the combined first velocity CEOF and the second temperature CEOF are similar to a solution of the linearized model in McCreary and Yu (1992). This model is a linearization of a non-linear 2-1/2 layer model with longitudinally variable wind stress and an upper layer that can entrain and detrain water. This model develops three different instabilities, two of which are antisymmetric about the equator in temperature and have periods of 21 and 35-53 days. In addition to having a similar period to the observed combined temperature and velocity CEOFs, the modeled 21-day instability is surface trapped with maxima out of phase in temperature

near  $2^{\circ}\text{N}$  and  $2^{\circ}\text{S}$  and dominated by meridional velocity on the equator. McCreary and Yu (1992) and Yu et al. (1995) identified the 21-day instability as a frontal instability that transforms mean potential energy associated with upper-layer meridional temperature gradients on both sides of the EUC to eddy potential energy. Yu et al. (1995) revisited the linear model from McCreary and Yu (1992), adding asymmetry in the mean currents, and concluded that the 21-day instability resulted from a combination of barotropic instability in the EUC-SEC shear and frontal instability.

The source of energy for the 20-day TIW is not as clear as that for the 30-day TIW. Yu et al. (1995) argue for a frontal instability on the northern flank of the EUC as the primary source of energy. However, observational analyses consistently find the main energy source for TIWs between the equator and  $2^{\circ}\text{N}$  to be from barotropic instability in the EUC-SECN shear (Hansen and Paul 1984; Luther and Johnson 1990; Qiao and Weisberg 1998). Non-linear models find energy conversion from both barotropic (Donohue and Wimbush 1998; Masina et al. 1999b) and frontal instabilities (McCreary and Yu 1992), as possible sources between the equator and  $2^{\circ}\text{N}$ . In a detailed analysis of the energetics of an 18-level non-linear model, Masina et al. (1999b) showed that the barotropic energy conversion near the equator was triggered by the baroclinic energy conversion between  $2^{\circ}\text{N}$  and  $4^{\circ}\text{N}$ . Whichever is the case, there is substantial evidence of at least two regions of TIW variability: the first between the equator and  $3^{\circ}\text{N}$  which is primarily from barotropic instability in the EUC-SECN shear and/or frontal instability and the other between  $2^{\circ}\text{N}$  and  $9^{\circ}$  which is likely from barotropic instability in the SECN-NECC shear but maybe partly or wholly due to baroclinic instability.



## 5. The Yanai wave

The 20-day fluctuations in meridional velocity at  $140^{\circ}\text{W}$  share some characteristics with the Yanai wave in a resting ocean, such as westward and upward propagation of phase, eastward and downward propagation of energy, an estimated zonal wavelength of 1320 km, anticyclonic motion off the equator and dominant meridional velocities on the equator (Halpern et al. 1988). However, the 20-day TIW described herein has an asymmetrical amplitude structure in temperature (Figure 12, bottom panels) that is inconstant with the symmetrical amplitude structure of a Yanai wave in a resting ocean (McPhaden and Knox 1979).

The addition of a mean zonal current alters the meridional structure of the Yanai wave. McPhaden and Knox (1979) examined the Yanai wave in the presence of mean zonal currents from the Central Pacific. Their analysis linearized the equations of motion about a geostrophically balanced mean zonal current in a 2-1/2 layer model, assumed a solution in the form of a zonally propagating wave, and then solved the resulting eigenvalue problem for solutions near zero wavenumber. They found that the Central Pacific currents increased the phase speed of the Yanai wave and shifted the maxima in the amplitude of perturbation zonal velocity closer to the equator but did not significantly alter perturbation meridional velocity or pressure.

Using the two-mode model and zonal currents from Lyman et al. (2004) described in section 4, the Yanai wave with a wavelength near the Halpern et al. (1988) estimate of 1320 km is examined. As in McPhaden and Knox (1979), the mean zonal currents decreased the period of the stable 1320-km Yanai wave from 20 days to 17 days and shifted the maxima in the amplitude of perturbation zonal velocity towards the equator (Figure 15). Additionally, there were significant changes to the perturbation temperature field resulting in larger amplitudes south of the equator

FIG. 15 (Figure 15).

The latitudinal structure of temperature and velocity of the observed 20-day TIW, with a 17-day period, is similar to the 17-day Yanai wave from the two-mode model. Like the modeled Yanai wave, the observed second temperature CEOF has out of phase maxima at  $2^{\circ}\text{N}$  and  $2^{\circ}\text{S}$  which are larger in the south (Figures 12 and 15). Although the degree of asymmetry across the equator is larger in the observations, most of the characteristics of the first velocity CEOF are the same as the Yanai wave at the equator; it is dominated by meridional velocity, surface intensified and leads temperature at  $2^{\circ}\text{S}$  by  $90^{\circ}$  (Figures 8, 12, 13, 15 and 16). These results show that the latitudinal and vertical structure in temperature, the period, the vertical structure of meridional velocity at the equator, and the phase relationship between temperature and meridional velocity for the 20-day TIW are consistent with a Yanai wave in the presence of a mean background current from the

FIG. 16 Central Pacific.

Surface trapped instabilities have been seen to generate Yanai waves that dissipated TIW energy below the thermocline in nonlinear models of the Central Pacific (Cox 1980; McCreary and Yu 1992; Masina et al. 1999a). Eriksen and Richman (1988) found observational evidence of Yanai wave energy below 500 meters in the Central Pacific consistent with this process. In particular, the surface trapped instabilities from McCreary and Yu (1992) which are similar to the 20-day TIW (section 4) generated Yanai waves in the non-linear version of their model. These instabilities provide a likely energy source for the stable Yanai wave.

The Reynolds stresses of the observed first velocity CEOF (Figure 8) are surface trapped, like the modeled 21-day unstable solution from McCreary and Yu (1992). There is also variability below the thermocline which is partly explained by the first mode CEOF of velocity but doesn't have an associated Reynolds stress (Figures 3 and 8). Similarly, south of the equator the observed

second CEOF of temperature explains a significant amount of the variability below the lower thermocline (Figure 12). This agreement between models and observations suggests that these CEOFs are a combination of a surface trapped instability and a propagating wave as proposed in Halpern et al. (1988).

## 6. Summary and Discussion

TIWs on the equator are consistently observed to have periods around 20 days, while near  $5^{\circ}\text{N}$  their period is estimated to be near 30 days. While the 20- and 30-day TIWs are prominent in the modeling literature, observation of their cross-equatorial structure has been limited to indirect observations from analysis of energetics or phase speed of an individual eddy. Observations of 20-day variability in off equator subsurface temperature presented in this paper are shown to be associated with velocity 20-day variability at the equator and separate from the 30-day signals previously observed in SSH and subsurface temperature.

The temperature and velocity data from the TAO moorings at  $140^{\circ}\text{W}$  are used to separate 20 from 30-day subsurface temperature variability. The spatial and temporal structures of these two physical modes of variability explain the latitudinal differences in TIW period. They are conveniently described from this data set by the first two temperature CEOFs and the first velocity CEOF.

The 30-day TIW is represented by the first CEOF of temperature (Figures 10 and 12, top panels). It is narrow-banded in frequency and resembles the  $n=1$ ,  $m=1$  unstable Rossby wave from Lyman et al. (2004) (Figure 14, top panel). Its maximum amplitude occurs at  $5^{\circ}\text{N}$  and is in phase across the equator. From previous modeling (Philander 1978; Cox 1980; Donohue and Wimbush 1998; Lyman et al. 2004) and observational studies (Luther and Johnson 1990; Baturin and Niiler 1997; Kennan 1997) the NECC-SECN shear appears to be the most likely source for the 30-day TIW. Although, baroclinic energy conversion might also provide a significant source of energy for the 30-day TIW (Cox 1980; Luther and Johnson 1990; Donohue and Wimbush 1998; Masina et al. 1999b; Lyman et al. 2004).

The 20-day TIW is made up of the second temperature CEOF (Figures 10 and 12, bottom panels) and the first velocity CEOF (Figures 8 and 6). It appears to be a combination of a stable Yanai wave and a surface trapped instability. As in the case of the stable Yanai wave in the presence of a mean zonal current (Figure 14 bottom panel), the temperature signature of the 20-day variability has maxima at  $2^{\circ}\text{N}$  and  $2^{\circ}\text{S}$  which are out of phase and larger in the south (Figure 12), while the velocity on the equator is dominated by meridional velocity, is stronger at the surface (Figure 8), and leads temperature at  $2^{\circ}\text{S}$  by  $90^{\circ}$  (Figure 13). This structure penetrates below the thermocline. Large Reynolds stresses, which are associated with the velocity CEOF at the surface, indicate the presence of instability at the surface which likely occurs from the EUC-SECN shear (Hansen and Paul 1984; Luther and Johnson 1990; Qiao and Weisberg 1998; Donohue and Wimbush 1998; Masina et al. 1999b) and/or frontal instability in the temperature front associated with the EUC (McCreary and Yu 1992).

It was possible to separate the 20-day from 30-day subsurface temperature variability because of the unique characteristics of the data used. First, the TAO array provides daily observations of temperature located near the maxima amplitudes of both the unstable Rossby wave and the Yanai wave. Second, these moorings are deployed on an ongoing basis and therefore captured a three-year record of consecutive La Niña conditions, increasing the frequency resolution of the spectral estimates. The location and quantity of the temperature and velocity moorings are adequate to separate and classify these two waves. However, the data are too sparse to determine zonal wavelength or energetics of the TIWs. Such a separation would be much harder if not impossible from satellite measurements of SSH. The current relevant satellite altimeters, TOPEX/Poseidon and Jason have repeat periods of approximately 10 days which are barely adequate to resolve the observed 17-day period of the stable Yanai wave. Additionally, the subsurface temperature vari-

ability at  $2^{\circ}\text{S}$  and  $2^{\circ}\text{N}$  has a small SSH signature compared to the SSH signal associated with the TIW signal at  $5^{\circ}\text{N}$ . This difference arises because of large changes in the Coriolis parameter and smaller variability in subsurface temperature at lower latitudes.

This study suggests that caution should be used when estimating the period of TIWs from cusps in the SST front just north of the equator. These cusps occur where the 20-day and 30-day TIWs explain equal amounts of the total variance in the thermocline (Figure 12). This assertion is supported by the broad-banded frequency content of SST from analysis of the TAO mooring at

**FIG. 17**  $2^{\circ}\text{N}$  and  $140^{\circ}\text{W}$  alone, with high energy at periods from 15 to 50 days (Figure 17).

Even though linearized models were able to reproduce the observations presented in this paper, TIWs are known to be highly non-linear (Kennan and Flament 2000). The periods observed here are 17 and 33 days which are near-multiples of each other suggesting a possible non-linear interaction between the Yanai wave and the unstable Rossby wave. Additionally, possible interaction between these two waves is evident from their annual modulation and their estimated zonal wavelengths, which are nearly identical.

*Acknowledgements.* John M. Lyman was a National Research Council fellow during this research. Additional support was provided by the NOAA Office of Ocean and Atmospheric Research and the NOAA Office of Global Programs. Helpful comments were provided by Dennis W. Moore, Michael J. McPhaden, Eric S. Johnson, Sean Kennan, and an anonymous reviewer.

#### REFERENCES

- Baturin, N. G. and P. P. Niiler, 1997: Effects of instability waves in the mixed layer of the equatorial Pacific. *J. Geophys. Res.*, **102**, 21,771–21,793.
- Bryden, H. L. and E. C. Brady, 1989: Eddy momentum and heat fluxes and their effects on the circulation of the equatorial Pacific ocean. *J. Mar. Res.*, **47**, 55–79.
- Chelton, D. B., M. G. Schlax, S. K. Esbensen, N. Thum, M. H. Freilich, F. J. Wents, C. L. Gentemann, and M. J. McPhaden, 2001: Observations of coupling between surface wind stress and sea surface temperature in the eastern tropical Pacific. *J. Climate*, **14**, 1479–1498.
- Chelton, D. B., M. G. Schlax, J. M. Lyman, and R. A. deSzoeke, 2004: The latitudinal structure of monthly variability in the tropical Pacific. *J. Phys. Oceanogr.*, **in prep.**
- Contreras, R. F., 2001: Long-term observation of Tropical Instability Waves. *unknown*, **in prep.**
- Cox, M. D., 1980: Generation and propagation of 30-day waves in a numerical model of the Pacific. *J. Phys. Oceanogr.*, **10**, 1168–1186.
- Davis, R. E., 1976: Predictability of sea surface temperature and sea level pressure anomalies over the North Pacific Ocean. *J. Phys. Oceanogr.*, **6**, 249–266.

- Donohue, K. A. and M. Wimbush, 1998: Model results of flow instabilities in the tropical Pacific Ocean. *J. Geophys. Res.*, **103**, 21,401–21,412.
- Emery, W. J. and R. E. Thomson, 1997: *Data Analysis Methods in Physical Oceanography*. Pergamon.
- Eriksen, C. C. and J. G. Richman, 1988: An estimate of equatorial wave energy flux at 9- to 90-day periods in the central Pacific. *J. Geophys. Res.*, **93**, 15,455–15,466.
- Flament, P. J., S. C. Kennan, R. A. Knox, P. P. Niiler, and R. L. Bernstein, 1996: The three-dimensional structure of an upper ocean vortex in the tropical Pacific Ocean. *Nature*, **383**, 610–613.
- Halpern, D., R. A. Knox, and D. S. Luther, 1988: Observations of 20-day meridional current oscillations in the upper ocean along the Pacific equator. *J. Phys. Oceanogr.*, **18**, 1514–1534.
- Hansen, D. V. and C. A. Paul, 1984: Genesis and effects of long waves in the equatorial Pacific. *J. Geophys. Res.*, **89**, 10431–10440.
- Hashizume, H., S.-P. Xie, W. T. Liu, and K. Takeuchi, 2001: Local and remote atmospheric response to tropical instability waves: A global view from space. *J. Geophys. Res.*, **106**, 10,173–10,185.
- Johnson, G. C., B. M. Sloyan, W. S. Kessler, and K. E. McTaggart, 2002: Direct measurements of upper ocean currents and water properties across the Tropical Pacific Ocean during the 1990s. *Prog. Oceanogr.*, **52**, 31–61.



- Kennan, S. C., 1997: *Observations of a Tropical Instability Vortex*. Ph.D. thesis, University of Hawaii, Honolulu, HI.
- Kennan, S. C. and P. J. Flament, 2000: Observations of a tropical instability vortex. *J. Phys. Oceanogr.*, **30**, 2277–2301.
- Legeckis, R., 1977: Long waves in the eastern equatorial Pacific Ocean: A view from a geostationary satellite. *Science*, **197**, 1179–1181.
- 1986: Long waves in the equatorial Pacific and Atlantic oceans during 1983. *Ocean-Air Interactions*, **1**, 1–10.
- Legeckis, R., E. Pichel, and G. Nesterczuk, 1983: Equatorial long waves in geostationary satellite observation and in a multichannel sea surface temperature analysis. *Bull. Am. Meteorol. Soc.*, **64**, 133–139.
- Luther, D. S. and E. S. Johnson, 1990: Eddy energetics in the upper equatorial Pacific during Hawaii-to-Tahiti Shuttle Experiment. *J. Phys. Oceanogr.*, **20**, 913–944.
- Lyman, J. M., D. B. Chelton, R. A. deSzoeke, and R. M. Samelson, 2004: Tropical instability waves as a resonance between equatorial Rossby waves. *J. Phys. Oceanogr.*, **submitted**.
- Malardé, J. P., P. D. Mey, C. Périgaud, and J. F. Minster, 1987: Observations of long equatorial waves in the Pacific ocean by Seasat altimetry. *J. Phys. Oceanogr.*, **17**, 2273–2279.
- Masina, S., G. Philander, and A. Bush, 1999a: An analysis of tropical instability waves in a numerical model of the Pacific ocean. Part I: Spatial variability. *J. Geophys. Res.*, **104**, 29,613–29,636.

- 1999b: An analysis of tropical instability waves in a numerical model of the Pacific ocean. Part II: Generation and energetics. *J. Geophys. Res.*, **104**, 29,637–29,662.
- McCreary, J. P. and Z. Yu, 1992: Equatorial dynamics in a 2.5-layer model. *Prog. Oceanogr.*, **29**, 61–132.
- McPhaden, M. J., 1996: Monthly period oscillations in the Pacific North Equatorial Countercurrent. *J. Geophys. Res.*, **16**, 6337–6359.
- McPhaden, M. J., A. J. Busalacchi, R. Cheney, J.-R. Donguy, K. S. Gage, D. Halpern, M. Ji, P. Julian, G. Meyers, G. T. Mitchum, P. P. Niiler, J. Picaut, R. W. Reynolds, N. Smith, and K. Takeuchi, 1998: The Tropical Ocean-Global Atmosphere observing system: a decade of progress. *J. Geophys. Res.*, **103**, 14,169–14,240.
- McPhaden, M. J. and R. A. Knox, 1979: Equatorial Kelvin and inertio-gravity waves in zonal shear flow. *J. Phys. Oceanogr.*, **9**, 263–277.
- Miller, L., D. R. Watts, and M. Wimbush, 1985: Oscillations of dynamic topography in the eastern equatorial Pacific. *J. Phys. Oceanogr.*, **15**, 1759–1770.
- Musman, S., 1989: Sea height wave form in equatorial waves and its interpretation. *J. Geophys. Res.*, **94**, 3303–3309.
- Périgaud, C., 1990: Sea level oscillations observed with Geosat along the two shear fronts of the Pacific North Equatorial Countercurrent. *J. Geophys. Res.*, **95**, 7239–7248.
- Philander, S. G. H., 1978: Instabilities of zonal equatorial currents, 2. *J. Geophys. Res.*, **83**, 3679–3682.

- Proehl, J. A., 1996: Linear stability of equatorial zonal flows. *J. Phys. Oceanogr.*, **26**, 601–621.
- 1998: The role of meridional flow asymmetry in the dynamics of tropical instability. *J. Geophys. Res.*, **103**, 24,597–24,618.
- Pullen, P. E., R. L. Bernstein, and D. Halpern, 1987: Equatorial long-wave characteristics determined from satellite Sea Surface Temperature and in situ data. *J. Geophys. Res.*, **92**, 742–748.
- Qiao, L. and R. H. Weisberg, 1995: Tropical instability wave kinematics: Observations from the Tropical Instability Wave Experiment. *J. Geophys. Res.*, **100**, 8677–8693.
- 1998: Tropical instability wave energetics: Observations from the Tropical Instability Wave Experiment. *J. Phys. Oceanogr.*, **28**, 345–360.
- Seidel, H. F. and B. S. Giese, 1999: Equatorial currents in the Pacific ocean 1992–1997. *J. Geophys. Res.*, **104**, 7849–7863.
- Strutton, P. G., J. P. Ryan, and F. P. Chavez, 2001: Enhanced chlorophyll associated with tropical instability waves in the equatorial Pacific. *Geophys. Res. Lett.*, **28**, 2005–2008.
- Xie, S.-P., M. Ishiwatari, H. Hashizume, and K. Takeuchi, 1998: Coupled ocean-atmospheric waves on the equatorial front. *Geophys. Res. Lett.*, **25**, 3863–3866.
- Yu, Z., J. P. McCreary, and J. A. Proehl, 1995: On the meridional asymmetry and energetics of tropical instability waves. *J. Phys. Oceanogr.*, **25**, 1680–1686.

**Figure Captions**

FIG. 1. TAO/TRITON Array mooring locations.

FIG. 2. Thirteen years of the SOI starting in 1980. Three consecutive years of La Niña conditions (shaded area) are analyzed here.

FIG. 3. Time-depth plots of filtered (a) meridional and (b) zonal velocities at 0°N, 140°W and unfiltered temperature at (c) 2°S, 140°W and (d) 5°N, 140°W.

FIG. 4. Frequency-depth plot of the log power spectral densities of filtered zonal velocities at 0°N, 140°W in units of  $(cm/sec)^2/cpd$ . The thick lines are for the 1998-2001 period and the thin line is for the TIWE period. The 1998-2001 spectra has been computed according to section 2, while the one year TIWE period as also been band averaged over 3 spectral estimates. Only spectral estimates greater than  $10^4 (cm/sec)^2/cpd$  are contoured.

FIG. 5. Variance of band-pass filtered meridional (solid line) and zonal (dashed line) velocities at 0°N, 140°W over the three year record beginning in April 1998.

FIG. 6. Amplitude (top panel), phase (middle panel), and real part (bottom panel) of the time series for the first two combined meridional and zonal velocity CEOFs. The first mode (thick lines) explains 63% of the total variance while the second mode (thin lines) explains 17%. Amplitude and the real part of the time series are multiplied by their maximum spatial amplitudes. Dashed lines in the middle panel correspond to periods of 17 and 33 days.

FIG. 7. Power spectral densities of the first (thick line) and second (thin line) velocity CEOFs from Figure 6 computed according to Section 2. Period in days is plotted on the top x-axis and noted for peaks.

FIG. 8. First velocity CEOF spatial amplitude (top left panel), phase (top right panel), percent variance explained (bottom left panel) for meridional (solid lines), and zonal (dashed lines) velocities, and Reynolds stress (bottom right panel).

FIG. 9. Variance of band-pass filtered temperature data at 140°W over a three-year period beginning in May 1998. Mean isotherms (white lines) from the same time period are overlaid. White dots show the TAO thermistor locations.

FIG. 10. CEOF analysis follows Figure 6, but for TAO temperature data along 140°W. The first mode explains 28% of the total variance while the second mode explains 13%. The missing section of the first-mode CEOF was excluded according to criteria described in Section 2.

FIG. 11. Power spectral density following Figure 7, except for the temperature time-series in Figure 10. The larger error bars are for the first CEOF, because the first year of that CEOF has a significant gap.

FIG. 12. Spatial modes for the first (top panels) and second (bottom panels) temperature CEOFs. Panels on the left show percent variance explained. Middle panels are the CEOF amplitude multiplied by the maxima of the amplitude time-series, contoured where at least 10% of the variance is explained. Panels on the right display CEOF phase, contoured where the scaled CEOF amplitude (middle panels) is exceeds 1°C. To match the phase in Figures 14 and 15 the phase for the first and second CEOFs have been shifted by  $-85^\circ$  and  $-144^\circ$  respectively.

FIG. 13. Lagged cross-correlation between real parts of the first velocity CEOF time series of velocity and the second temperature CEOF time series. For positive lags, temperature leads velocity. Dashed vertical lines drawn at  $\pm 4.25$  days and dashed horizontal lines at 95% confidence level.

FIG. 14. Depth-latitude plots of amplitude (left panel) and phase (right panel) of the temperature solution for the  $n=1$ ,  $m=1$  unstable Rossby wave from Lyman et al. (2004). This solution has a 31-day period, a 1384-km wavelength and a 68-day e-folding time. Meridional and zonal velocities are not shown.

FIG. 15. Depth-latitude plots of amplitude (left panels) and phase (right panels) of the  $n=1$  Yanai wave with a 17-day period and a 1320-km wavelength from Lyman et al. (2004). Top panels show temperature ( $C^\circ$ ); middle panels show zonal velocity ( $cm s^{-1}$ ); and bottom panels show meridional velocity ( $cm s^{-1}$ ). Temperature has been estimated from pressure by assuming a constant thermal expansion coefficient of  $1200 \times 10^{-7} K^{-1}$ , so that velocity and temperature are scaled approximately the same.

FIG. 16. Depth profile of meridional velocity (solid line) and zonal velocity (dashed line) of the Yanai wave at the equator from the two-mode projection model.

FIG. 17. As in Figure 7, except for 1-m temperatures at 2°N, 140°W from the TAO mooring. Because of large gaps, the time series has been broken into three 262-day sections and Hanning windowed.

Figures

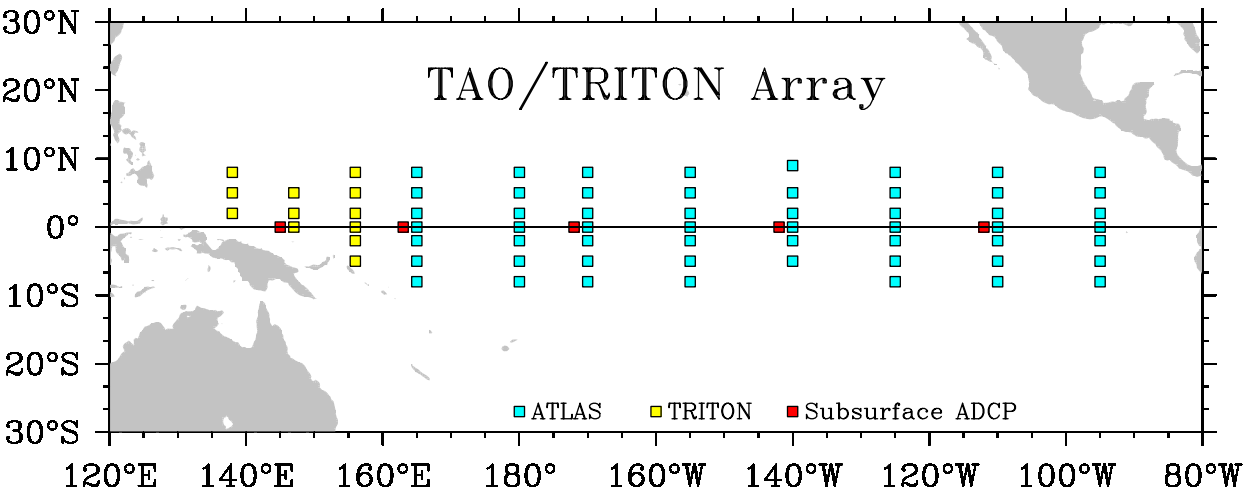


FIG. 1. TAO/TRITON Array mooring locations.

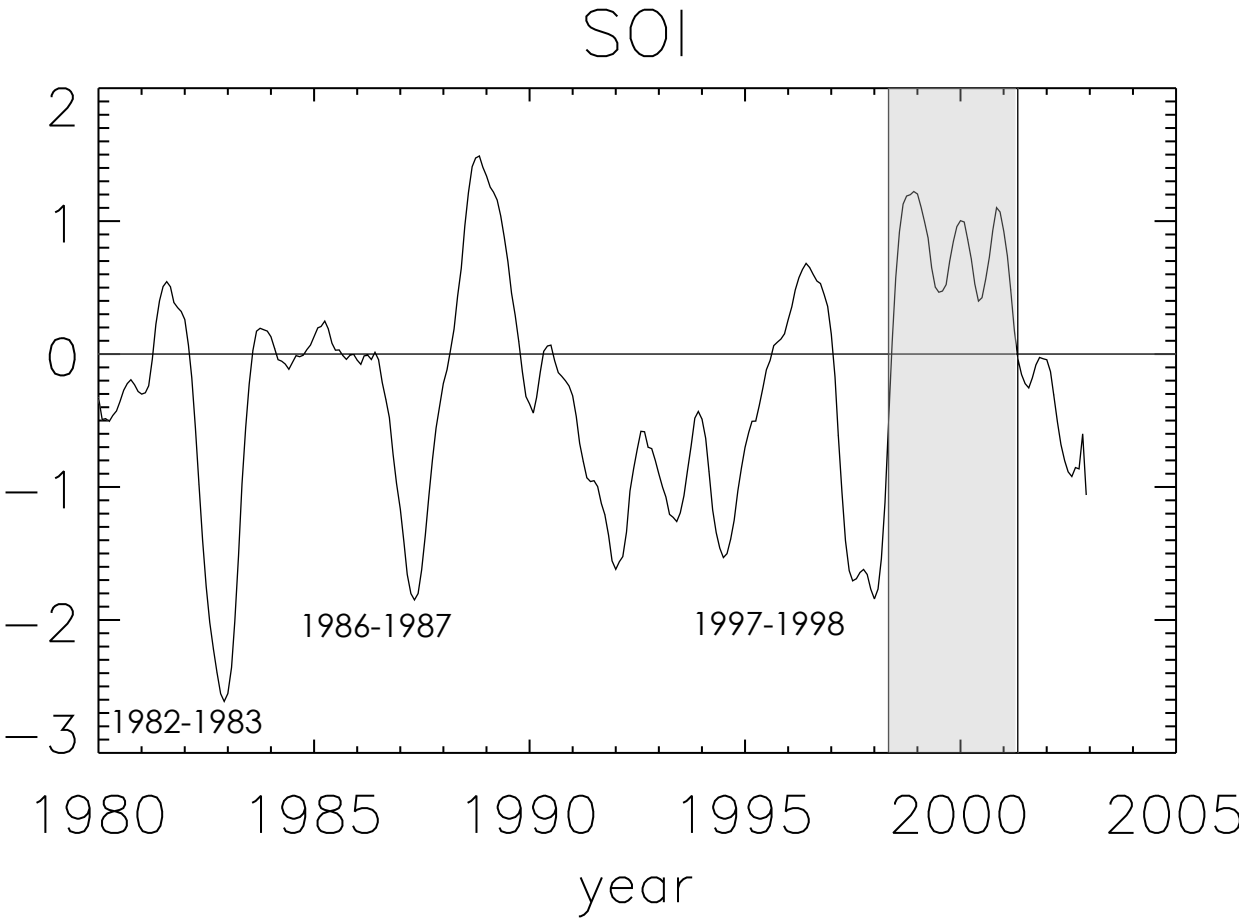


FIG. 2. Thirteen years of the SOI starting in 1980. Three consecutive years of La Niña conditions (shaded area) are analyzed here.

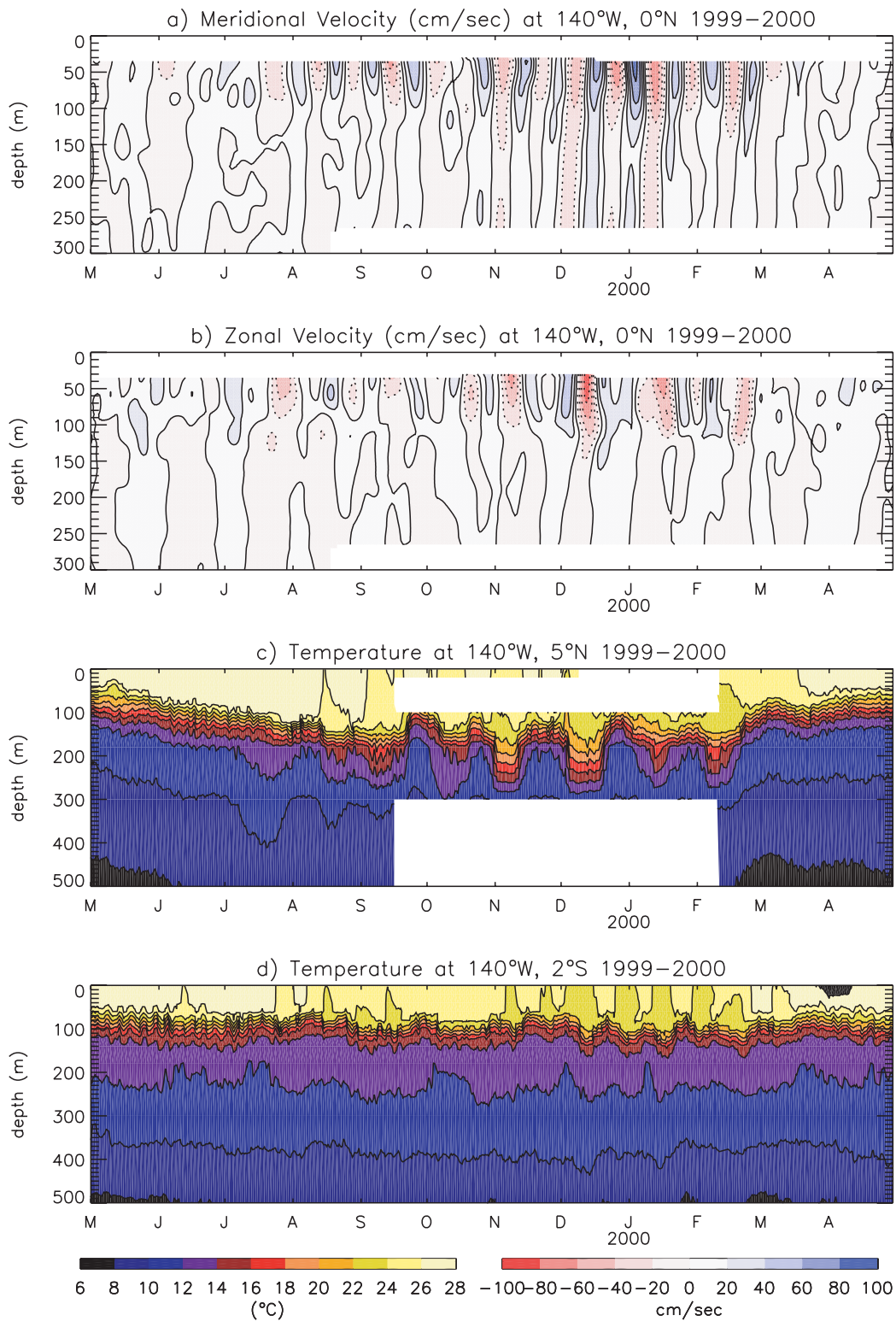


FIG. 3. Time-depth plots of filtered (a) meridional and (b) zonal velocities at 0°N, 140°W and unfiltered temperature at (c) 2°S, 140°W and (d) 5°N, 140°W.



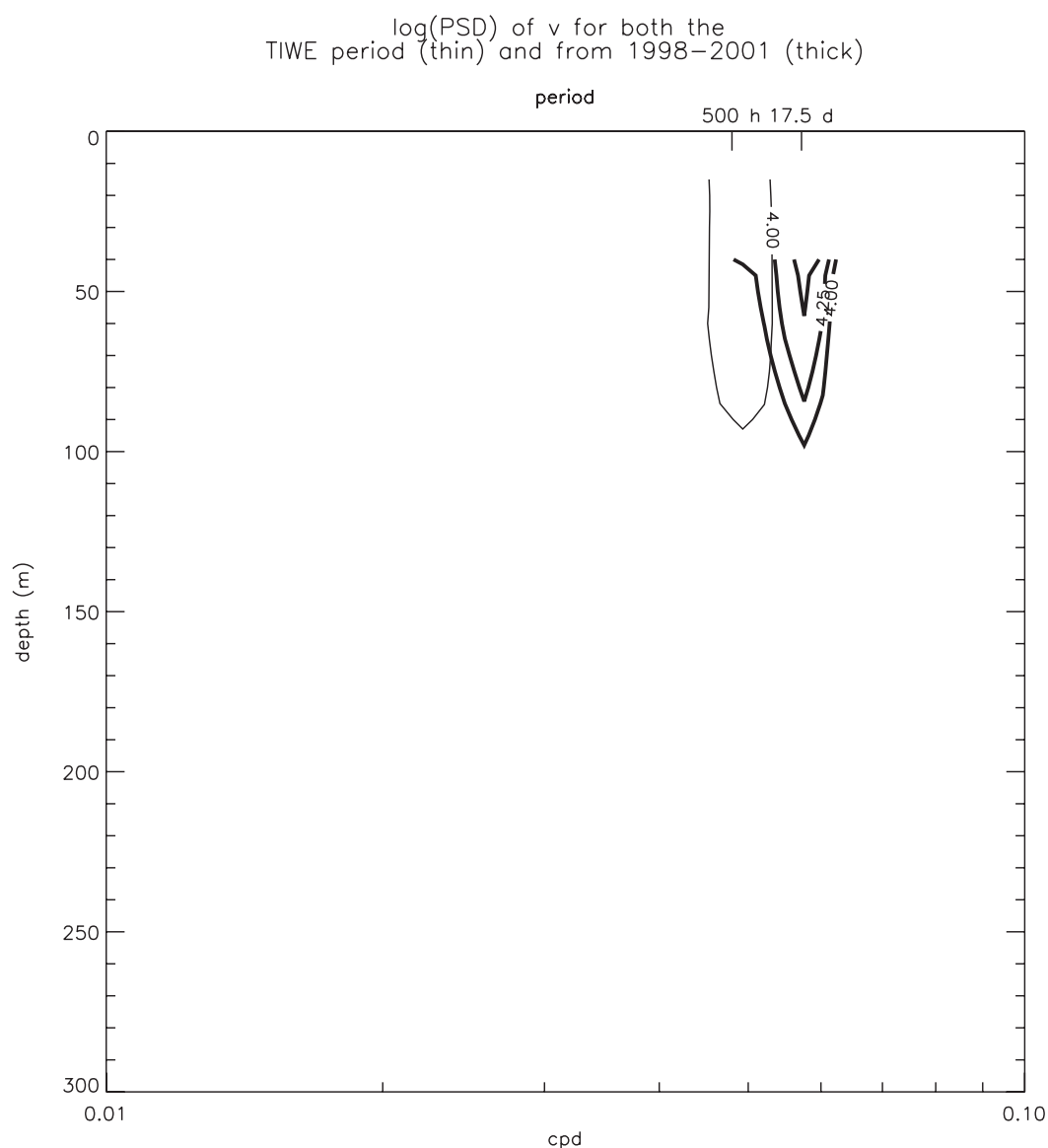


FIG. 4. Frequency-depth plot of the log power spectral densities of filtered zonal velocities at  $0^{\circ}\text{N}$ ,  $140^{\circ}\text{W}$  in units of  $(\text{cm}/\text{sec})^2/\text{cpd}$ . The thick lines are for the 1998–2001 period and the thin line is for the TIWE period. The 1998–2001 spectra has been computed according to section 2, while the one year TIWE period as also been band averaged over 3 spectral estimates. Only spectral estimates greater than  $10^4 (\text{cm}/\text{sec})^2/\text{cpd}$  are contoured.

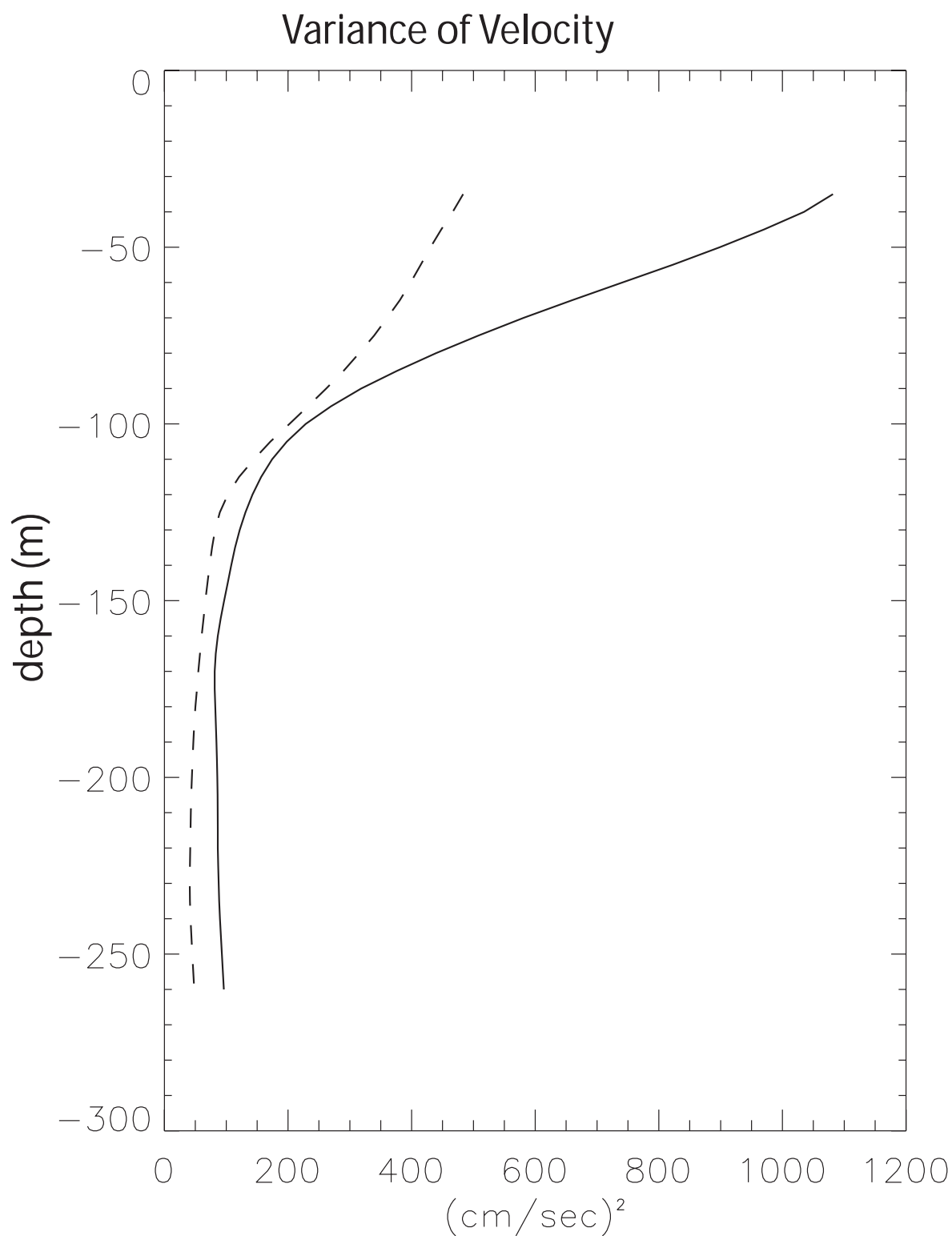


FIG. 5. Variance of band-pass filtered meridional (solid line) and zonal (dashed line) velocities at  $0^{\circ}\text{N}$ ,  $140^{\circ}\text{W}$  over the three year record beginning in April 1998.

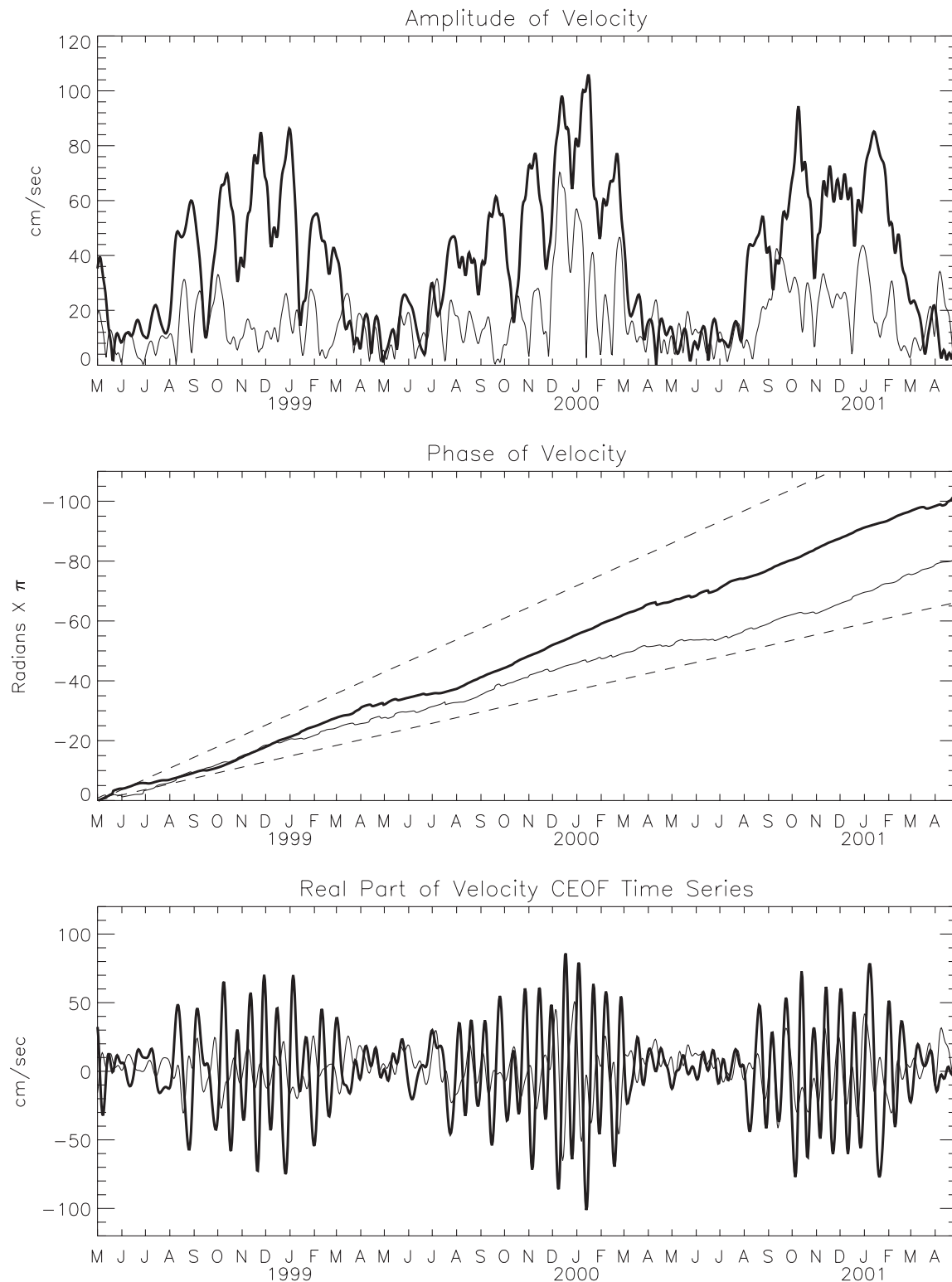


FIG. 6. Amplitude (top panel), phase (middle panel), and real part (bottom panel) of the time series for the first two combined meridional and zonal velocity CEOFs. The first mode (thick lines) explains 63% of the total variance while the second mode (thin lines) explains 17%. Amplitude and the real part of the time series are multiplied by their maximum spatial amplitudes. Dashed lines in the middle panel correspond to periods of 17 and 33 days.

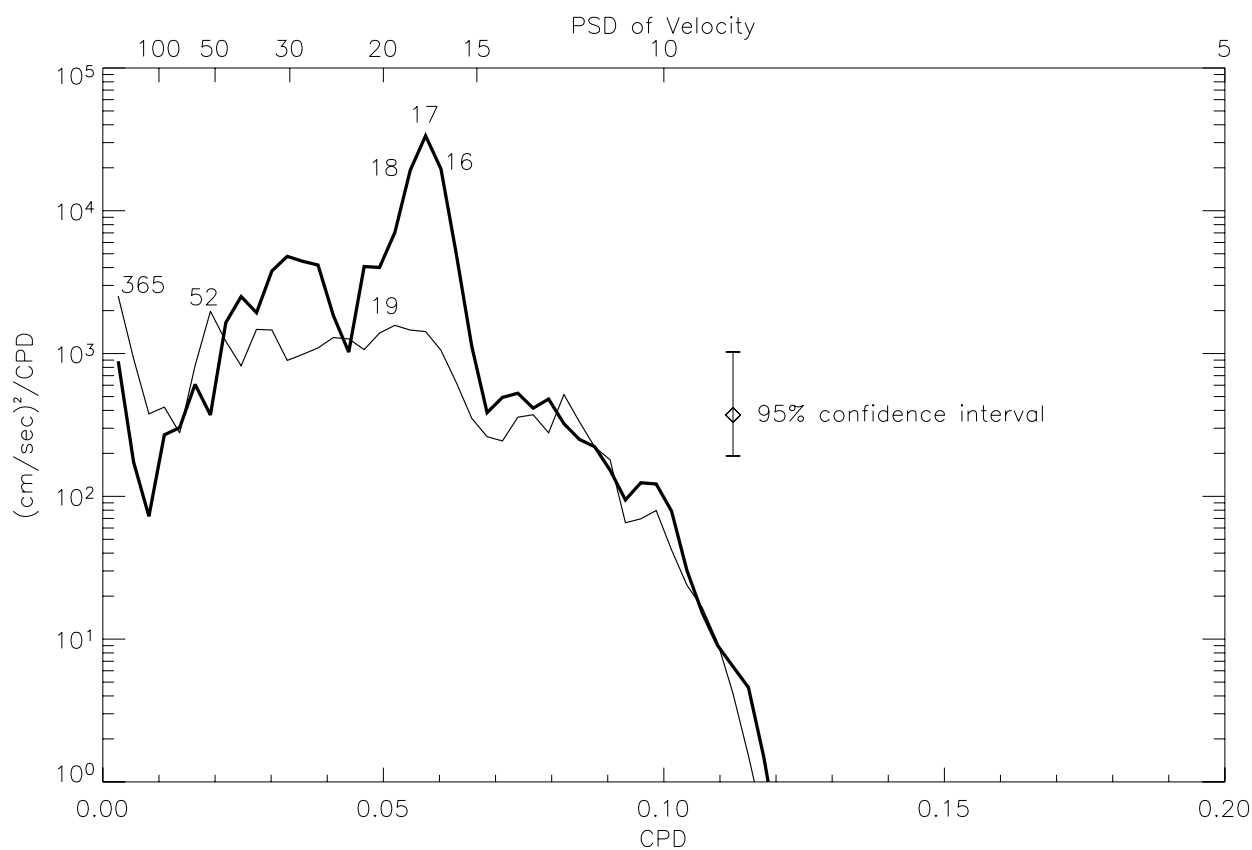


FIG. 7. Power spectral densities of the first (thick line) and second (thin line) velocity CEOFs from Figure 6 computed according to Section 2. Period in days is plotted on the top x-axis and noted for peaks.

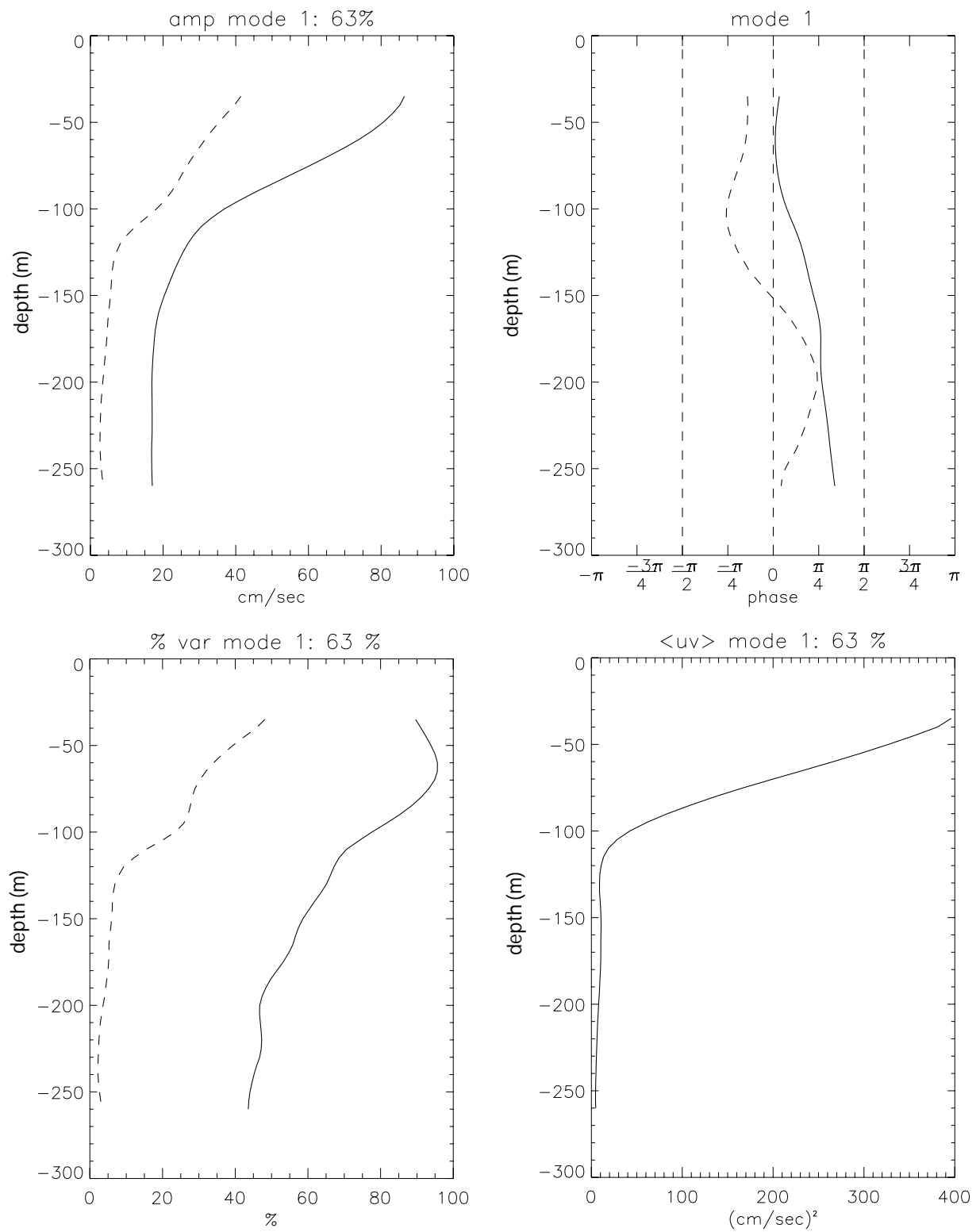


FIG. 8. First velocity CEOF spatial amplitude (top left panel), phase (top right panel), percent variance explained (bottom left panel) for meridional (solid lines), and zonal (dashed lines) velocities, and Reynolds stress (bottom right panel).

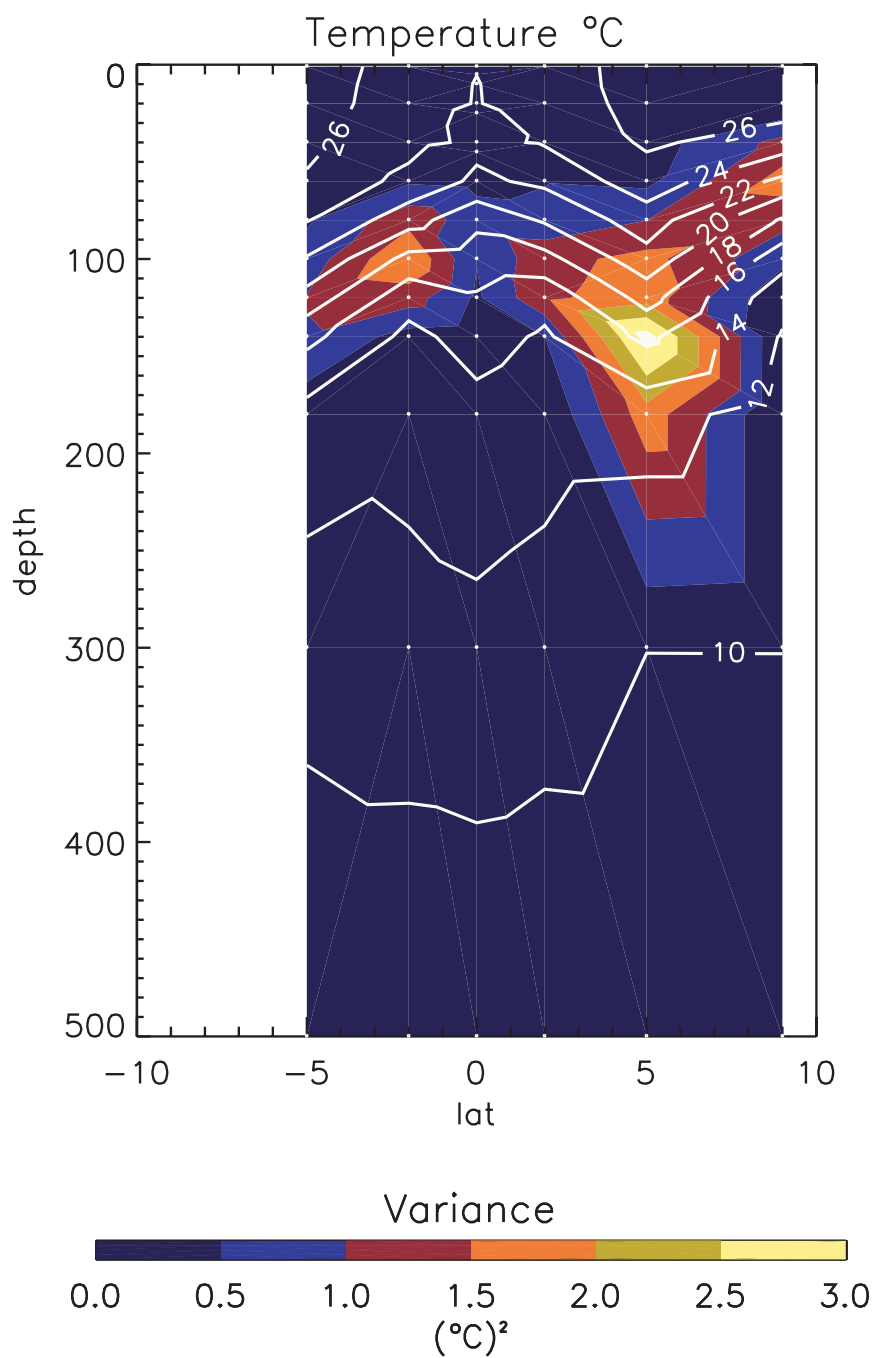


FIG. 9. Variance of band-pass filtered temperature data at 140°W over a three-year period beginning in May 1998. Mean isotherms (white lines) from the same time period are overlaid. White dots show the TAO thermistor locations.

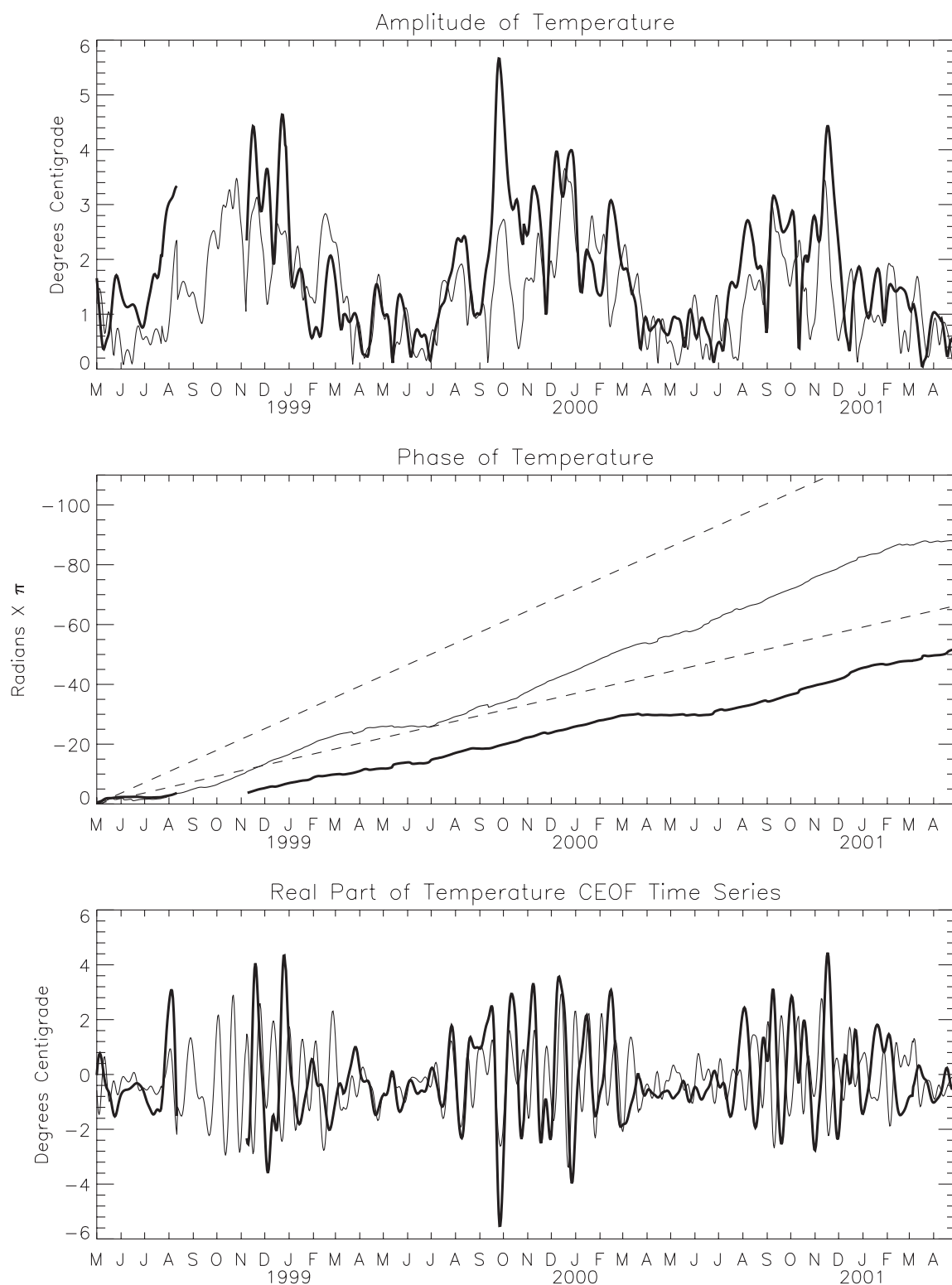


FIG. 10. CEOF analysis follows Figure 6, but for TAO temperature data along  $140^{\circ}\text{W}$ . The first mode explains 28% of the total variance while the second mode explains 13%. The missing section of the first-mode CEOF was excluded according to criteria described in Section 2.

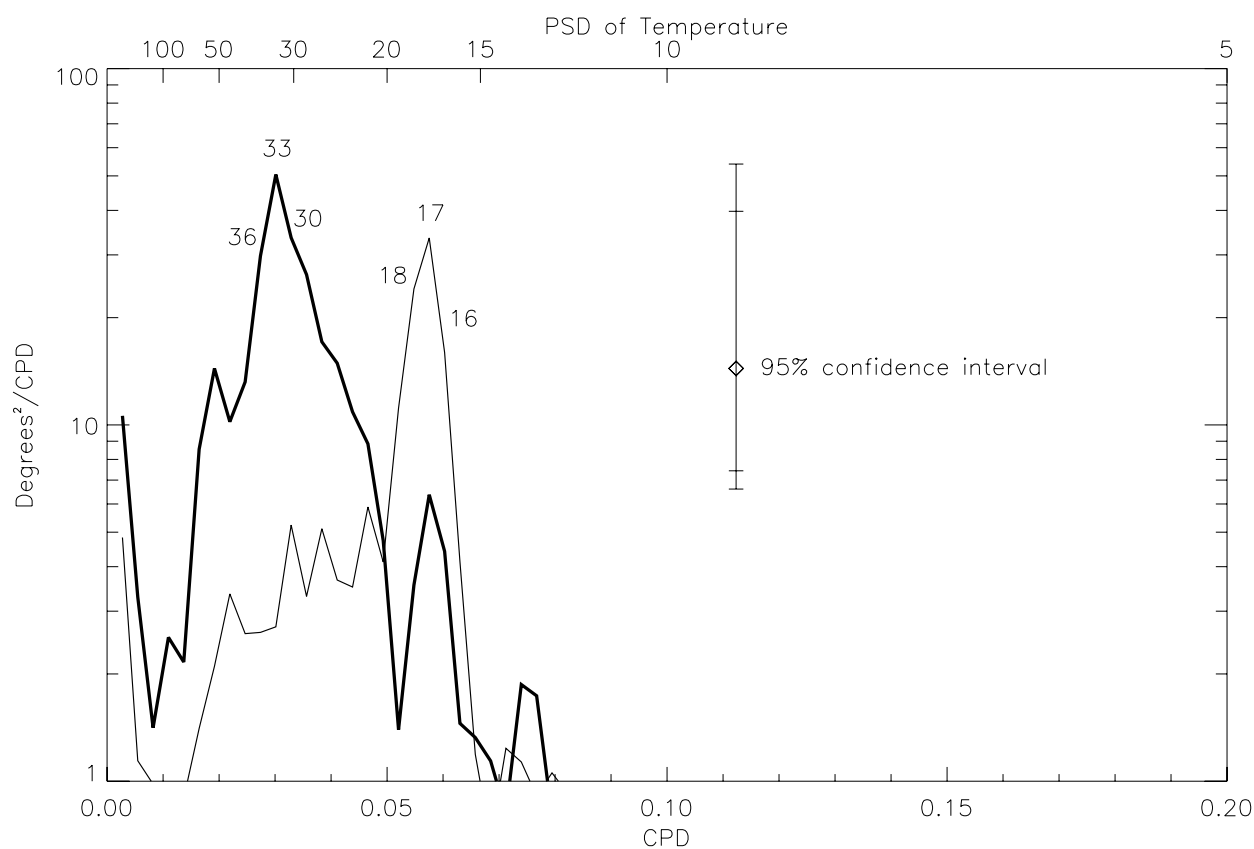


FIG. 11. Power spectral density following Figure 7, except for the temperature time-series in Figure 10. The larger error bars are for the first CEOF, because the first year of that CEOF has a significant gap.



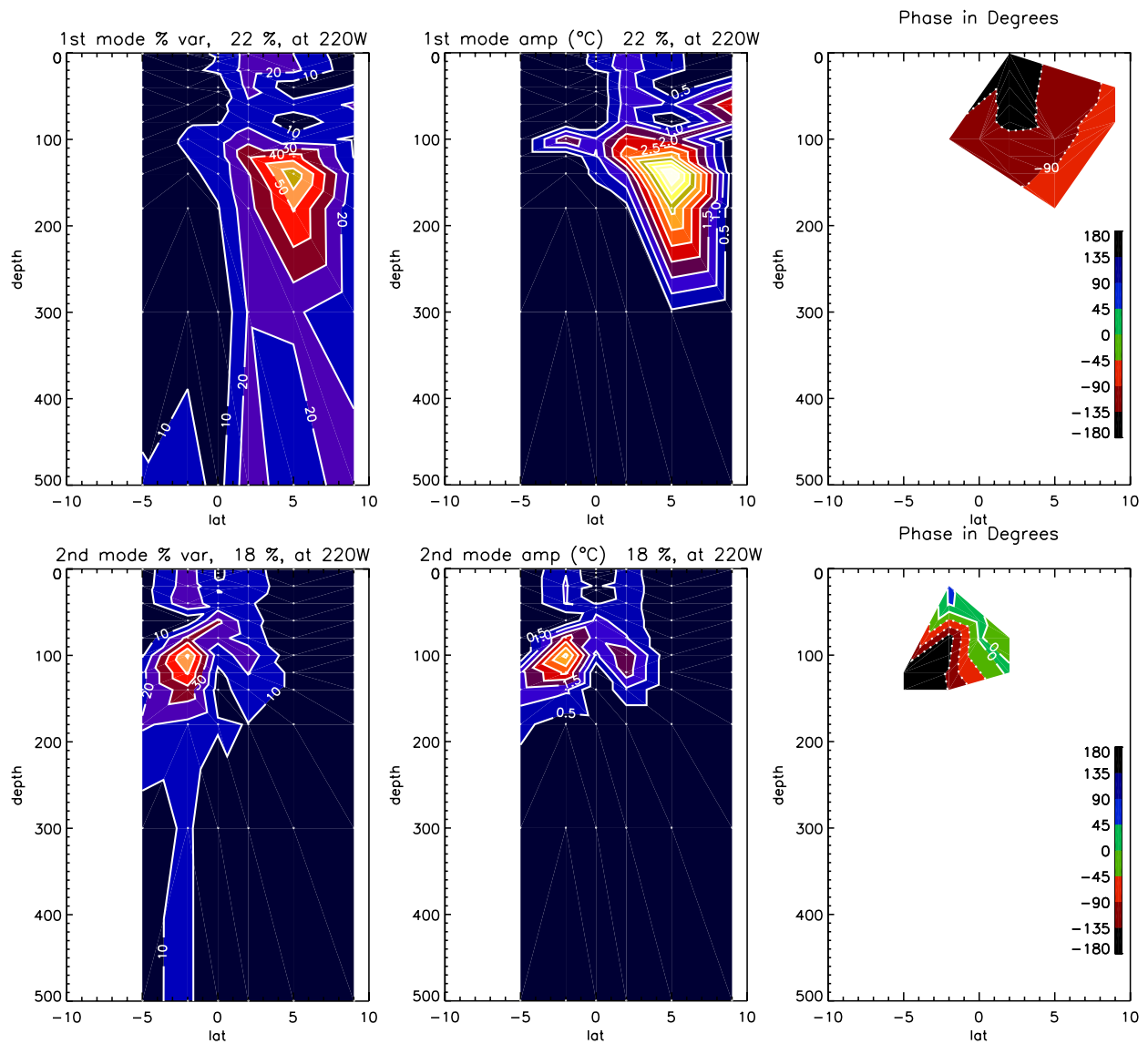


FIG. 12. Spatial modes for the first (top panels) and second (bottom panels) temperature CEOFs. Panels on the left show percent variance explained. Middle panels are the CEOF amplitude multiplied by the maxima of the amplitude time-series, contoured where at least 10% of the variance is explained. Panels on the right display CEOF phase, contoured where the scaled CEOF amplitude (middle panels) is exceeds  $1^\circ\text{C}$ . To match the phase in Figures 14 and 15 the phase for the first and second CEOFs have been shifted by  $-83^\circ$  and  $-144^\circ$  respectively.

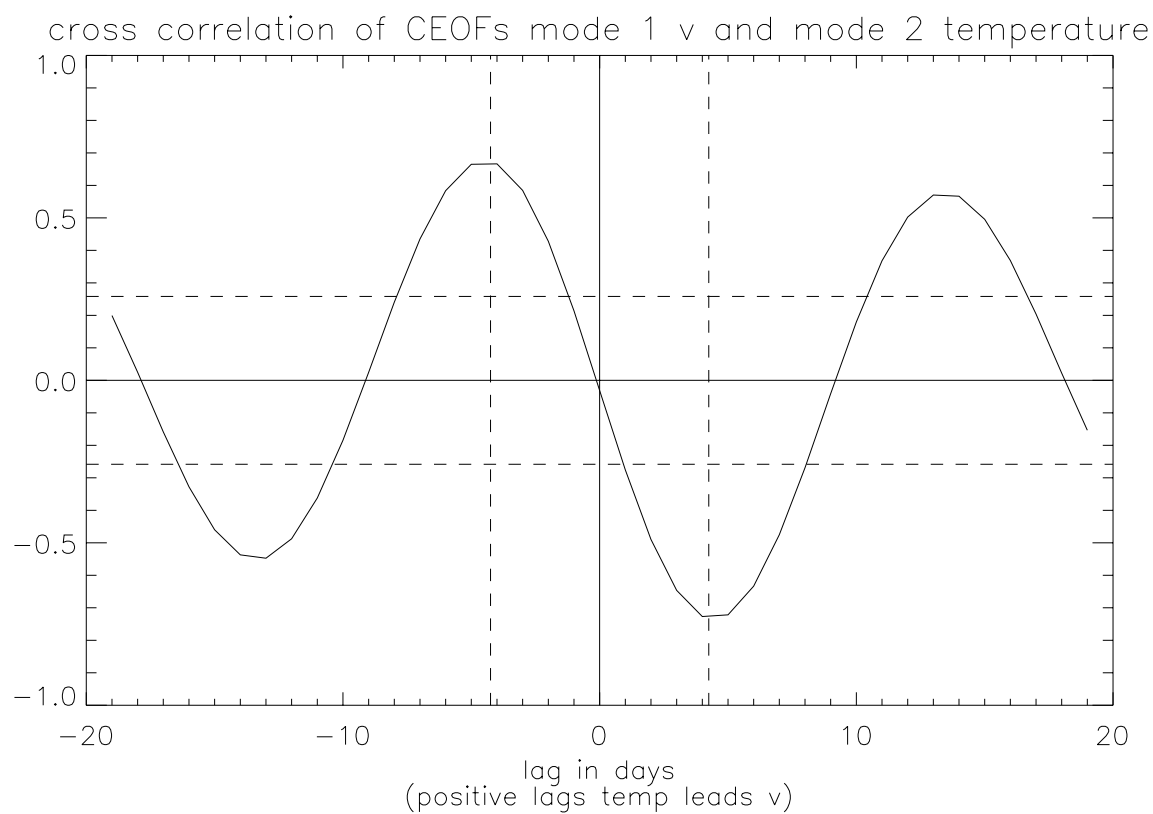


FIG. 13. Lagged cross-correlation between real parts of the first velocity CEOF time series of velocity and the second temperature CEOF time series. For positive lags, temperature leads velocity. Dashed vertical lines drawn at  $\pm 4.25$  days and dashed horizontal lines at 95% confidence level.

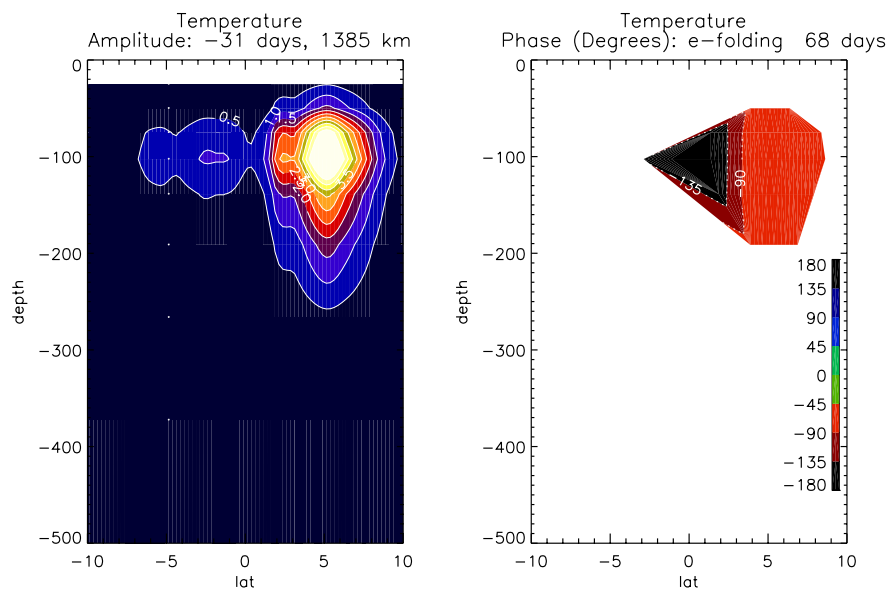


FIG. 14. Depth-latitude plots of amplitude (left panel) and phase (right panel) of the temperature solution for the  $n=1, m=1$  unstable Rossby wave from Lyman et al. (2004). This solution has a 31-day period, a 1384-km wavelength and a 68-day e-folding time. Meridional and zonal velocities are not shown.

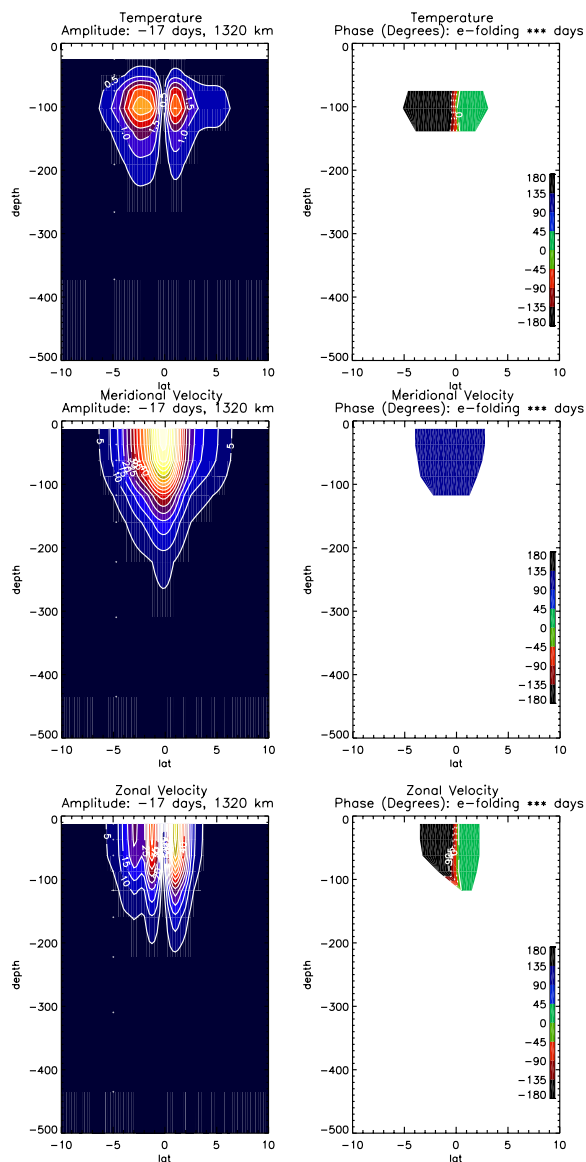


FIG. 15. Depth-latitude plots of amplitude (left panels) and phase (right panels) of the  $n=1$  Yanai wave with a 17-day period and a 1320-km wavelength from Lyman et al. (2004). Top panels show temperature ( $^{\circ}\text{C}$ ); middle panels show zonal velocity ( $\text{cm s}^{-1}$ ); and bottom panels show meridional velocity ( $\text{cm s}^{-1}$ ). Temperature has been estimated from pressure by assuming a constant thermal expansion coefficient of  $1200 \times 10^{-7} \text{ K}^{-1}$ , so that velocity and temperature are scaled approximately the same.

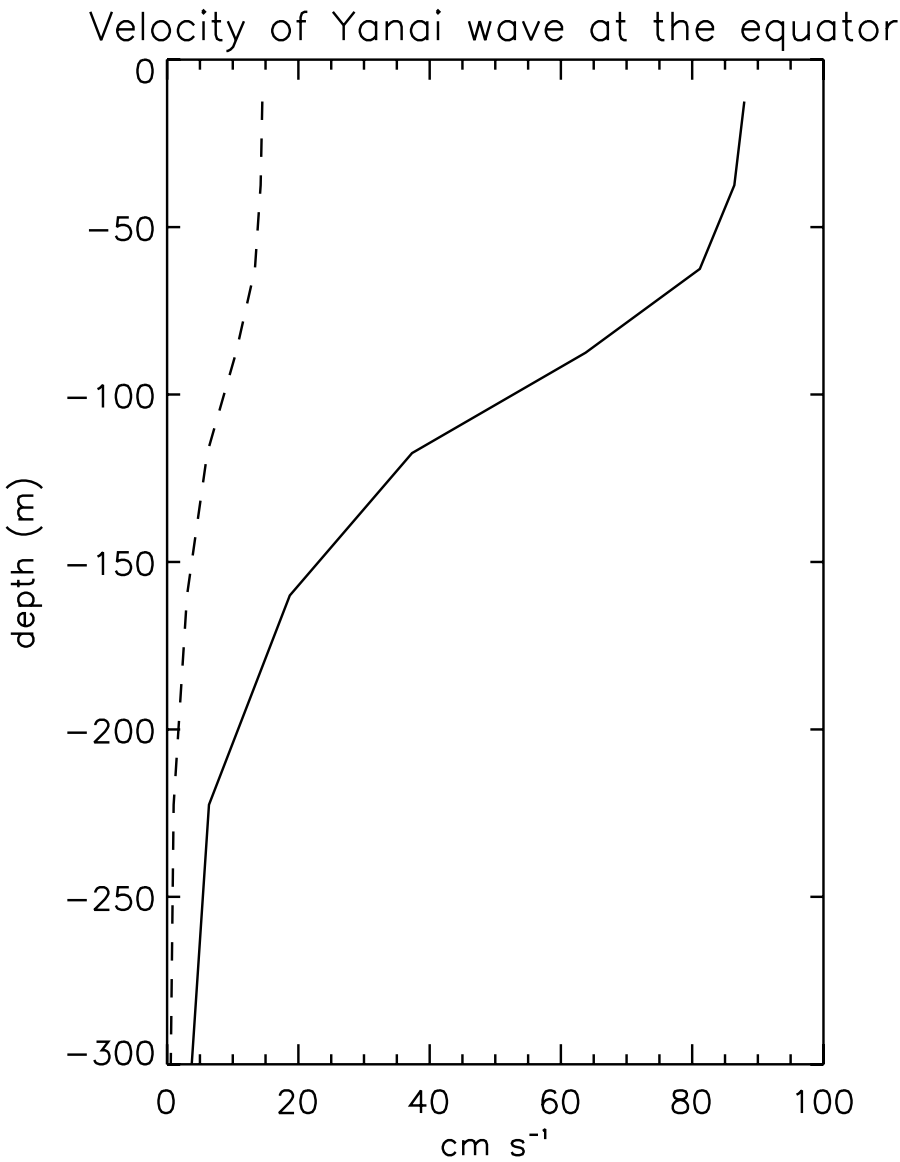


FIG. 16. Depth profile of meridional velocity (solid line) and zonal velocity (dashed line) of the Yanai wave at the equator from the two-mode projection model.

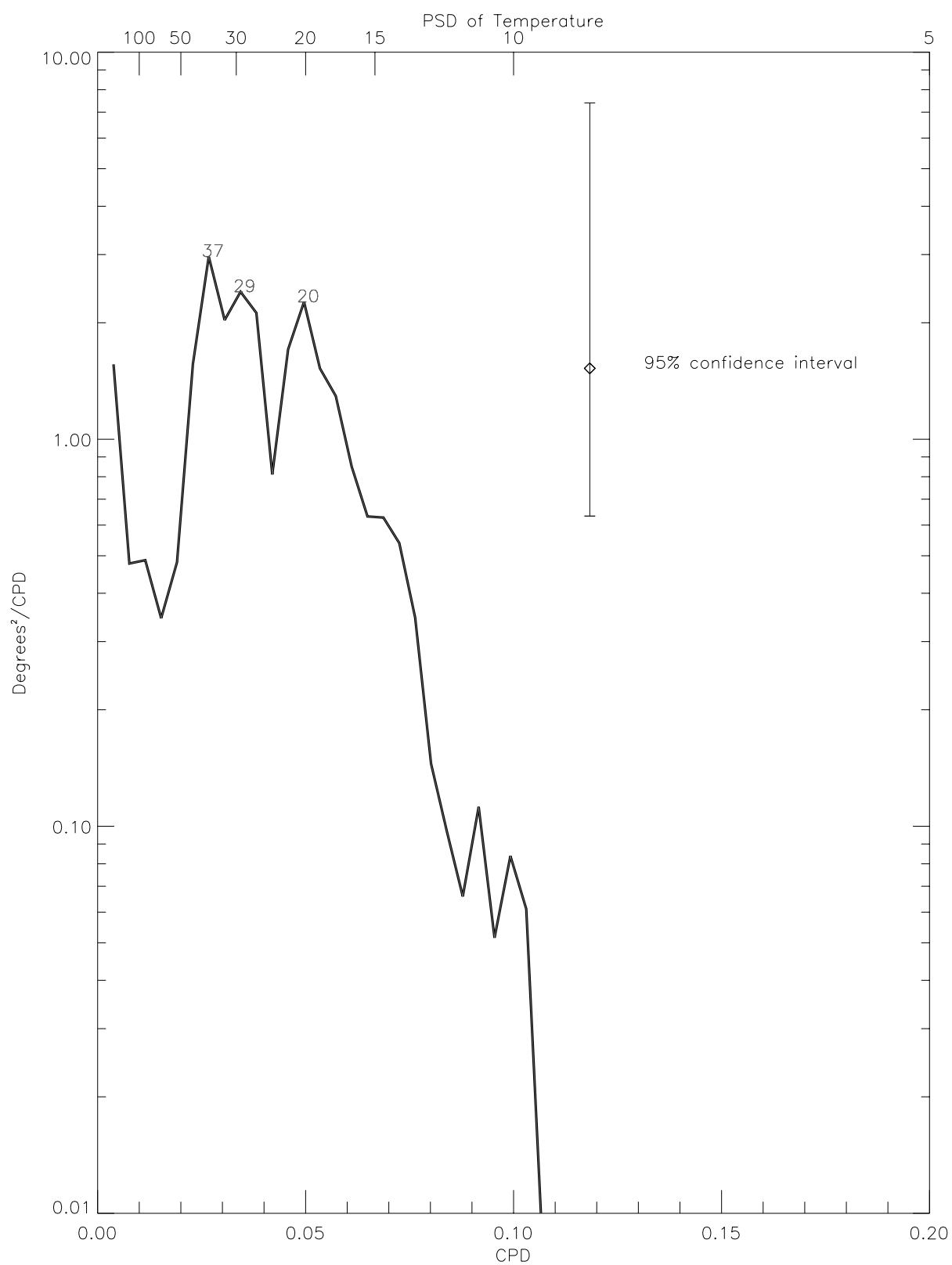


FIG. 17. As in Figure 7, except for 1-m temperatures at 2°N, 140°W from the TAO mooring. Because of large gaps, the time series has been broken into three 262-day sections and Hanning windowed.